Check for updates

ADVANCED FUNCTIONAL MATERIALS
www.afm-journal.de

Printed and Stretchable Triboelectric Energy Harvester Based on P(VDF-TrFE) Porous Aerogel

Karem Lozano Montero, Remmi Calvo Guzman, Amit Tewari, Haiyang Zou, Zhong Lin Wang, Matti Mäntysalo, and Mika-Matti Laurila*

Developing energy harvesting devices is crucial to mitigate the dependence on conventional and rigid batteries in wearable electronics, ensuring their autonomous operation. Nanogenerators offer a cost-effective solution for enabling continuous operation of wearable electronics. Herein, this study proposes a novel strategy that combines freeze-casting, freeze-drying, and printing technologies to fabricate a fully printed triboelectric nanogenerator (TENG) based on polyvinylidene fluorid-etrifluoroethylene P(VDF-TrFE) porous aerogel. First, the effects of porosity and poling on the stretchability and energy harvesting capabilities of P(VDF-TrFE) are investigated, conducting a comprehensive analysis of this porous structure's impact on the mechanical, ferroelectric, and triboelectric properties compared to solid P(VDF-TrFE) films. The results demonstrate that structural modification of P(VDF-TrFE) significantly enhances stretchability increasing it from 7.7% (solid) to 66.4% (porous). This modification enhances output voltage by 66% and generated charges by 48% for non-poled P(VDF-TrFE) porous aerogel films compared to their non-poled solid counterparts. Then, a fully printed TENG is demonstrated using stretchable materials, exhibiting a peak power of 62.8 mW m^{-2} and an average power of 9.9 mW m^{-2} over 100 tapping cycles at 0.75 Hz. It can illuminate light-emitting diodes (LEDs) through the harvesting of mechanical energy from human motion. This study provides a significant advance in the development of energy harvesting devices.

1. Introduction

The continuous growth in the field of wearable electronics has led to remarkable advancements in health monitoring, smart accessories, and personalized technology solutions. Owing to their multifunctionality and adaptability in a wide range of applications, wearables have been used for monitoring and gathering data from the human body for fitness or medical applications.[1] A significant constraint is that most wearable electronics rely on bulky and rigid batteries to power the necessary electronics for collecting, handling, and sending data, also making integration and attachment to the human body challenging. Therefore, an essential requirement for next-generation wearables is the ability to generate and store energy autonomously, ensuring prolonged usage without the need for frequent recharging or battery replacement.[2] Various energy harvesting mechanisms have been proposed as cost-effective solutions for the development of self-powered wearables. These mechanisms include mechanical energy harvesting, solar energy harvesting, thermal energy harvesting, and biochemical energy harvesting.[3] The use of mechanical energy harvesting systems is a promising solution for wearable electronics as it allows, for example, harvesting the mechanical energy generated by the human body motion.[4] Nanogenerators (NG), which can convert mechanical energy into electricity, can address the energy requirements of wearable electronics.[5]

K. Lozano Montero, R. Calvo Guzman, A. Tewari, M. Mäntysalo, M.-M. Laurila
Faculty of Information Technology and Communication Sciences
Tampere University
Tampere 33720, Finland
E-mail: karem.lozanomontero@tuni.fi

The ORCID identification number(s) for the author(s) of this article can be found under https://doi.org/10.1002/adfm.202312881

© 2024 The Authors. Advanced Functional Materials published by Wiley-VCH GmbH. This is an open access article under the terms of the Creative Commons Attribution License, which permits use, distribution and reproduction in any medium, provided the original work is properly cited.

DOI: 10.1002/adfm.202312881

K. Lozano Montero, H. Zou, Z. L. Wang
School of Materials Science and Engineering
Georgia Institute of Technology
Atlanta, GA 30318, USA

H. Zou
College of Materials Science and Engineering
Sichuan University
Chengdu 610065, China

Z. L. Wang
Beijing Institute of Nanoenergy and Nanosystems
Chinese Academy of Sciences
Beijing 101400, P. R. China

Notably, triboelectric nanogenerators (TENGs), based on triboelectrification and electrostatic induction have shown high energy conversion of low-frequency mechanical excitations (e.g., human walking and body motion).[6,7] To ensure their usability, TENGs must seamlessly integrate into packaging that enables direct attachment to the skin or integration into clothing,[8,9] while maintaining characteristics such as softness, stretchability or flexibility, and lightweight properties.[10] Material selection is pivotal in enhancing TENG functionality by introducing features like flexibility and stretchability, thereby significantly improving their energy output.[11] Furthermore, structural modification in TENGs, involving the creation of surface irregularities and morphological changes in the triboelectric materials, serves to increase the active contact surface area with the opposite contact pair, further optimizing their efficiency and performance.[12]

In addition to TENGs, piezoelectric nanogenerators (PENGs) can harvest the electricity generated by mechanical deformation of piezoelectric materials. Piezoelectric polymers, such as polyvinylidene fluoride (PVDF) and its copolymers, have previously been proposed for fabricating PENGs.[13–16] However, the output power of PENGs using solid piezoelectric polymers is relatively limited.[17,18] Additionally, their compatibility with wearable or on-skin applications is restricted due to the non-stretchable nature of these materials, which typically exhibit a strain no >10%.[19,20] To address some of these challenges, porous materials based on P(VDF) and polyvinylidene fluoride-trifluoroethylene (P(VDF-TrFE)) have been engineered and these have been reported to combine piezo and triboelectric phenomena with stretchability.[21–23] Nonetheless, the extent of stretchability and the primary source of charge generation (whether piezoelectric, triboelectric, or both) in these materials has not been comprehensively studied. Furthermore, developing scalable fabrication processes for energy harvesters based on these materials is of utmost importance, as the application area (i.e., powering Internet of Things (IoT) devices) requires fabricating billions of such devices.[24] Various printing technologies, including doctor blade coating, inkjet printing, screen printing, and 3D printing, have been demonstrated as cost-effective approaches for the development of flexible and stretchable electronics.[25–29]

This study aims to investigate the solution to these challenges by 1) presenting a fabrication process for P(VDF-TrFE) porous aerogel 2) investigating the stretchability and the origin of increased power output (piezoelectric or triboelectric, or both) in a P(VDF-TrFE) porous aerogel layer and 3) presenting a printing-based and scalable fabrication process for a TENG device based on the P(VDF-TrFE) porous aerogel. Specifically, the P(VDF-TrFE) porous aerogel film was prepared by 1) freezing doctor blade-coated P(VDF-TrFE) (i.e., P(VDF-TrFE) powder dissolved in dimethyl sulfoxide (DMSO)), 2) solvent removal, and 3) freeze-drying of the film. The piezoelectricity of the porous film was characterized to investigate if the piezoelectric properties of the P(VDF-TrFE) porous aerogel have an impact on the triboelectric output. The use of the porous film as triboelectric material and the effect of the polarization of the P(VDF-TrFE) porous aerogel film was studied by pairing it with polymers of different polarities, including polyethyleneterephalate (PET), polyimide (PI), thermoplastic polyurethane (TPU), and Ecoflex. We also determined the optimal polarization state of P(VDF-TrFE) for maximizing electrical output by analyzing its role in various contact pair configurations. The results indicate a 60% to 70% improvement in the triboelectric charge generation of non-poled P(VDF-TrFE) porous aerogel compared to the solid film. However, the triboelectric effect in the solid P(VDF-TrFE) can be amplified to the same level by inducing the piezoelectric effect through the poling step.

Finally, a TENG device based on the fabricated P(VDF-TrFE) porous aerogel film was assembled to demonstrate its energy harvesting capabilities. The device was fabricated using printing technologies, specifically doctor blade coating and 3D printing, and incorporated stretchable materials TPU, Ecoflex, P(VDF-TrFE) porous aerogel, and stretchable silver ink. Under a low frequency of 0.75 Hz, the TENG can generate a voltage of 105.6 ± 10.8 V and a charge of 35.8 ± 2.2 nC. **Table 1** shows the comparison of the main features of solution-based triboelectric nanogenerators, including the device developed in this study and state-of-the-art devices. The TENG fabricated using the P(VDF-TrFE) porous aerogel/Ecoflex contact pair is distinguished by its attributes as it is both printed and stretchable. It also demonstrates a peak power of 62.8 mW m^{-2} and an average power of 9.9 mW m^{-2}, showcasing promising performance relative to other studies. This is especially noteworthy when considering the characterization frequency. The latter comparison point is essential for TENGs designed for harvesting energy from low-frequency mechanical stimuli (biomechanical stimuli between 0.3 and 3.5 Hz),[30] as the peak power of the TENG can be optimized by increasing the characterization frequency. This frequency dependency can significantly impact the overall power output and efficiency of the devices, necessitating careful consideration in comparative evaluations.[31] In summary, the developed P(VDF-TrFE) porous aerogel shows great potential for biomechanical energy harvesting, and the TENG may be used for harvesting mechanical energy generated from body motion.

2. Results and Discussion

2.1. Formation of P(VDF-TrFE) Porous Aerogel

The fabrication process for both solid and P(VDF-TrFE) porous aerogel films is illustrated in **Figure 1a**. The chosen solvent plays a crucial role in promoting the formation of a porous structure during the fabrication process: choosing a high melting point solvent, such as DMSO (19°C), enables rapid freezing of the film at relatively high temperatures;[38] for comparison, another common P(VDF-TrFE) solvent, dimethylformamide (DMF) exhibits a significantly lower melting point of −61 °C. The solvent crystallizes when freezing the blade-coated solution below the DMSO melting temperature which results in P(VDF-TrFE) accumulation between the growing ice crystals through the phase separation process.[39,40] The frozen DMSO can be then removed by solvent-exchange, which involves immersing the frozen films in DI-water, resulting in the replacement of the solvent by water and the final solidification of P(VDF-TrFE).[40] The freeze-drying technique can be then used to remove the water from the sample by sublimation (i.e., direct transition from solid to gas state of a substance). The scanning electron microscopy (SEM) images of the top surface of a solid and a P(VDF-TrFE) porous aerogel films are shown in Figure 1b,c for comparative analysis. It can be seen that the presented fabrication process yields randomly

© 2024 The Authors. Advanced Functional Materials published by Wiley-VCH GmbH

16163028, 0, Downloaded from https://onlinelibrary.wiley.com/doi/10.1002/adfm.202312881 by Tampere Universitaet Foundation, Wiley Online Library on [23/02/2024]. See the Terms and Conditions (https://onlinelibrary.wiley.com/terms-and-conditions) on Wiley Online Library for rules of use; OA articles are governed by the applicable Creative Commons License

Table 1. Comparison of solution-based triboelectric nanogenerators. *Stretchable = considers if the device is fabricated using only stretchable materials.

Contact pairs	Printed	Stretchable*	Aerogel	Peak power	Average power	Frequency	Ref.
P(VDF-TrFE) – Ecoflex	Yes	Yes	Yes	62.8 mW m^{-2}	9.9 mW m^{-2}	0.75 Hz	This work
CNF – PDMS	Yes	No	Yes	29 mW m^{-2}	not reported	4 Hz	[32]
CNF/PEI – PVDF	No	No	Yes	13.3 W m^{-2}	not reported	10 Hz	[33]
Cellulose – PTFE	No	No	Yes	127 mW m^{-2}	not reported	1 Hz	[34]
CTS – PI	No	No	Yes	4.5 W m^{-2}	not reported	20 Hz	[35]
Sulfo/PSI – PFA	No	No	Yes	225 mW m^{-2}	not reported	3 Hz	[36]
BC/HEC – PVDF	No	No	Yes	7.91 mW m^{-2}	not reported	1 Hz	[37]

distributed porous structures throughout the film and increases the film's surface roughness. The solid P(VDF-TrFE) film exhibited a dry thickness of ≈27 µm, whereas the porous aerogel had a thickness of ~183 µm. This thickness disparity resulted from the 85% porosity of the P(VDF-TrFE) porous aerogel. For details regarding sample weights and porosity calculations, please refer to Section S3 (Supporting Information). Additionally, the surface profile of solid and P(VDF-TrFE) porous aerogel films is displayed in Figure 1d. The surface roughness average (R_a) for both films is depicted in Figure 1e. As observed in Figure 1b, the solid P(VDF-TrFE) film shows a smooth and uniform surface, resulting in an R_a value of 0.16 ± 0.02 µm. In contrast, the porous film exhibits an R_a value of 3.3 ± 0.7 µm, confirming the presence of pores on the film.

2.2. Stretchability

The mechanical properties of the porous and solid P(VDF-TrFE) films were examined through stress-strain curve analysis, providing valuable insights into their responses to mechanical stress. Within the stress-strain curves, clear differences appeared between the two film types as illustrated in Figure 1f. Young's modulus (E) was calculated from the linear part of the stress (σ)–strain (ϵ) curve as follows:

$$E = \frac{\sigma}{\epsilon} \quad (1)$$

This parameter represents the material's stiffness: the higher Young's modulus is, the stiffer the material is, while a lower

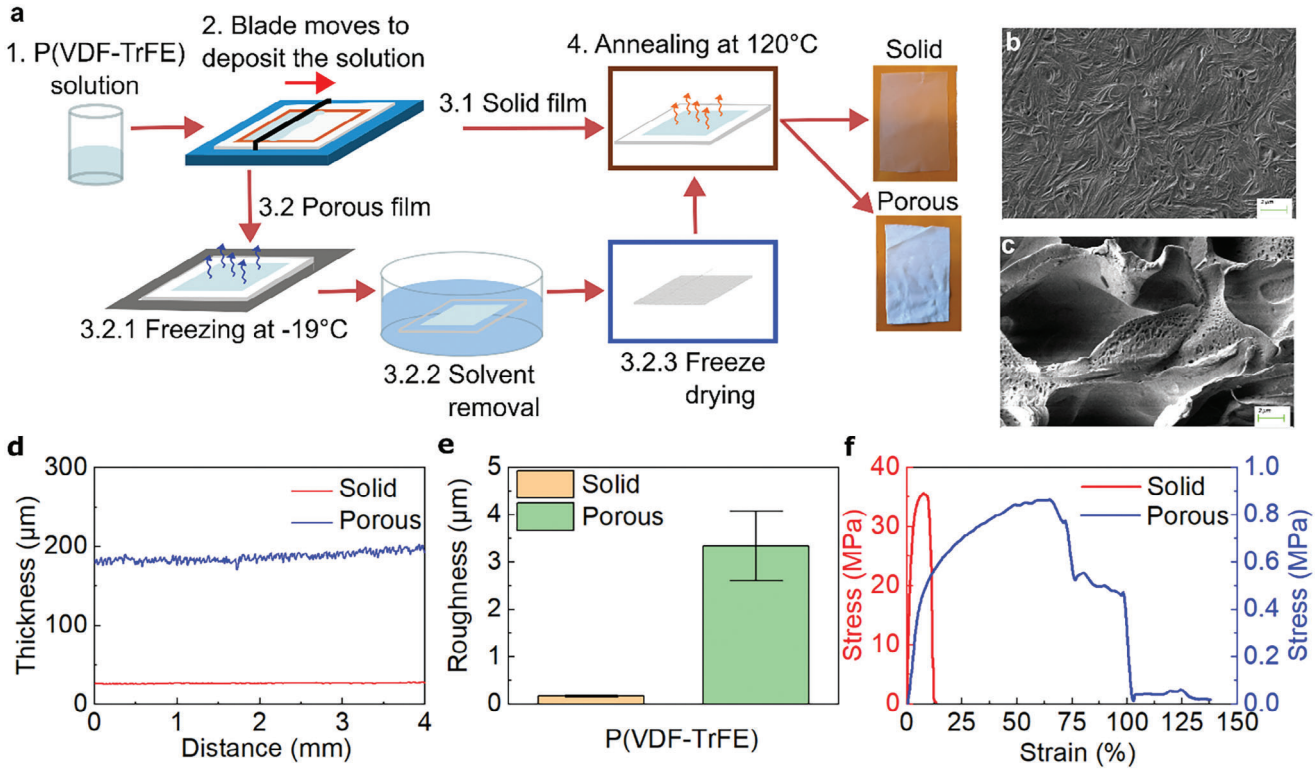

Figure 1. Fabrication process and surface and mechanical characterization. a) Fabrication steps of solid and P(VDF-TrFE) porous aerogel films. b,c) SEM image of solid and P(VDF-TrFE) porous aerogel film surface. d) Thickness of a solid and P(VDF-TrFE) porous aerogel films. e) Surface roughness average. The error bars represent one standard deviation above and below the mean, indicating the range of variability in the data. f) Stress–strain curve of solid and P(VDF-TrFE) porous aerogel films.

© 2024 The Authors. Advanced Functional Materials published by Wiley-VCH GmbH

16163028, 0, Downloaded from https://onlinelibrary.wiley.com/doi/10.1002/adfm.202312881 by Tampere Universitaet Foundation, Wiley Online Library on [23/02/2024]. See the Terms and Conditions (https://onlinelibrary.wiley.com/terms-and-conditions) on Wiley Online Library for rules of use; OA articles are governed by the applicable Creative Commons License

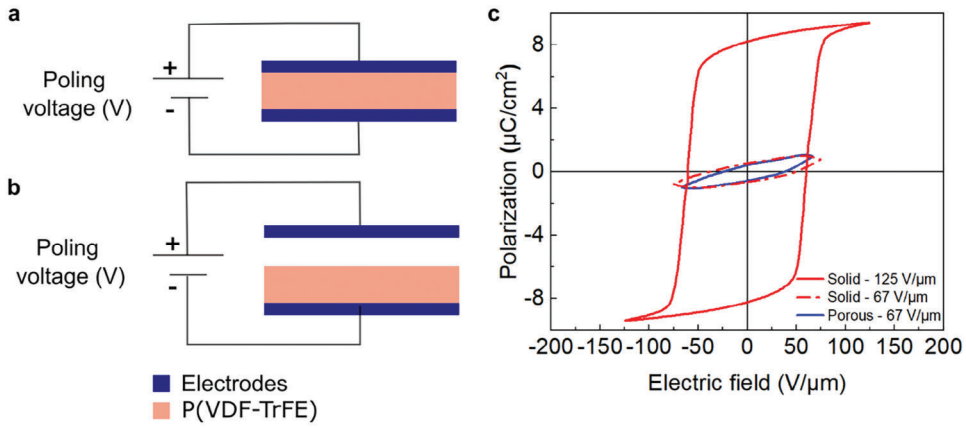

Figure 2. a) Contact poling schematic diagram, the top electrode is in direct contact with the P(VDF-TrFE) film surface. b) Corona poling schematic diagram, there is a gap between the top electrode and the P(VDF-TrFE) film surface. c) PE-loops for solid and P(VDF-TrFE) porous aerogel.

value indicates more flexibility and greater deformation at a given stress. The determination of the Young's modulus yielded contrasting values: the P(VDF-TrFE) porous aerogel film exhibited a Young's modulus of 7.2 MPa, while the solid P(VDF-TrFE) film displayed a significantly higher Young's modulus of 1281.4 MPa. Furthermore, the strain at break highlighted distinct characteristics: the porous film demonstrated a strain at a break of 66.4% at 0.9 MPa stress, whereas the solid film showed a more limited strain at a break of 7.7% under a notably higher stress of 35.6 MPa. These differences highlight the diverse mechanical behaviors of the porous and solid P(VDF-TrFE) films, hinting at the potential use of the porous film in applications that require stretchability. It is especially noteworthy that the stretchability of the P(VDF-TrFE) porous aerogel film exceeds the requirements for on-skin applications, where the maximum stretching has been measured to be 33.3% (at the knee joint).[41]

2.3. Ferroelectric and Piezoelectric Performance

The pristine P(VDF-TrFE) exhibits a net polarization of zero due to the random orientation of the dipoles in the material's crystallites. To enhance the piezoelectric properties, a poling process is employed to align these dipoles, thus creating remanent polarization (P_r) (i.e., polarization in the absence of an external electric field). The poling process involves applying an electric field over the bulk of the material. In this study, the samples were first poled using contact poling (i.e., P(VDF-TrFE) film sandwiched between two electrodes (**Figure 2**a)). The polarization-electric field hysteresis loop (PE-loop) of the solid and the P(VDF-TrFE) porous aerogel were measured to investigate the ferroelectric properties of the films. The PE-loop is the representation of the measured polarization (i.e., charges collected over the effective electrode area) while applying a high electric field. The measured PE-loops are illustrated in Figure 2c. For the solid P(VDF-TrFE) film, a maximum poling field of 125 V μm^{-1} resulted in a remanent polarization of 8.2 $\mu C\ cm^{-2}$. As for the P(VDF-TrFE) porous aerogel, the maximum poling field was limited by the dielectric breakdown of the film to 67 V μm^{-1} which resulted in a P_r of only 0.4 $\mu C\ cm^{-2}$. However, this is not significantly different when compared to the P_r value of the solid P(VDF-TrFE) at the same poling field (0.5 $\mu C\ cm^{-2}$). This indicates that the P(VDF-TrFE) in both cases has a very similar ferroelectric response and therefore crystalline structure (see also Section 2.3.1). We can therefore conclude that the main limiting factor in achieving a high P_r-value for the P(VDF-TrFE) porous aerogel is related to the dielectric breakdown which prevents poling at a sufficiently high electric field, and this leads to incomplete polarization (Section 2.3.2 provides a detailed analysis of the poling effect on the porous film). In conclusion, contact poling can yield a superior ferroelectric response in the solid P(VDF-TrFE) compared to the P(VDF-TrFE) porous aerogel film.

Furthermore, corona poling (Figure 2b) was used to investigate if the piezoelectric properties of the P(VDF-TrFE) porous aerogel could be achieved by an alternative poling method resulting in a cellular space charge electret effect. The poling was done to achieve different polarization states, namely, positive-poled, and negative-poled films. The piezoelectric sensitivity of the P(VDF-TrFE) porous aerogel films was then measured before and after poling to investigate the piezoelectric response of the films. The piezoelectric characterization is explained in more detail in Section S6 (Supporting Information). In a non-poled state, the P(VDF-TrFE) porous aerogel showed a piezoelectric sensitivity of 0.3 ± 0.2 pC N^{-1}. Nevertheless, the piezoelectric sensitivity after poling was only: 0.1 ± 0.04 pC N^{-1} for positive-poled P(VDF-TrFE) porous aerogel and 0.2 ± 0.2 pC N^{-1} for negative-poled P(VDF-TrFE) porous aerogel. For reference, the piezoelectric sensitivity of a solid P(VDF-TrFE) film (poled via contact poling) with different polarization states was also characterized. The piezoelectric sensitivity of the non-poled solid P(VDF-TrFE) was −0.2 ± 0.1 pC N^{-1}, which increased to 27.2 ± 1.7 pC N^{-1} when positive-poled and to −27.0 ± 0.9 pC N^{-1} when negative-poled. Thus, the piezoelectric properties of the solid P(VDF-TrFE) were enhanced after the poling process. In contrast, these results indicate that the piezoelectric response of the P(VDF-TrFE) porous aerogel could not be achieved with corona poling either. In addition to the characterization of the piezoelectricity after poling, the effect of the corona poling on the triboelectric performance of the porous films was also investigated as presented in Section 2.4.

It is generally acknowledged that the ferro- and piezoelectric performance of P(VDF-TrFE) is affected by the crystallinity and

© 2024 The Authors. Advanced Functional Materials published by Wiley-VCH GmbH

16163028, 0, Downloaded from https://onlinelibrary.wiley.com/doi/10.1002/adfm.202312881 by Tampere Universitaet Foundation, Wiley Online Library on [23/02/2024]. See the Terms and Conditions (https://onlinelibrary.wiley.com/terms-and-conditions) on Wiley Online Library for rules of use; OA articles are governed by the applicable Creative Commons License

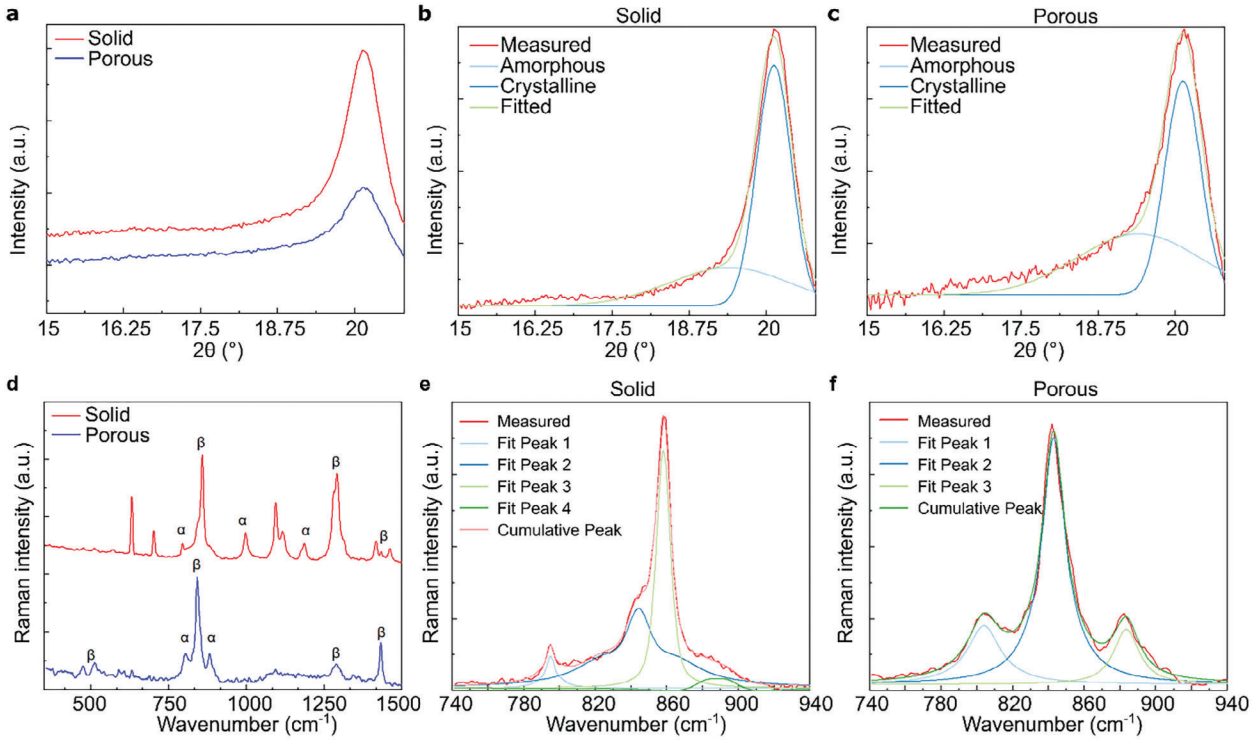

Figure 3. Crystallinity, and crystalline phases of the porous and solid P(VDF-TrFE) films. a) XRD pattern of solid and P(VDF-TrFE) porous aerogel films. b,c) Deconvolution of the XRD pattern of solid and P(VDF-TrFE) porous aerogel. d) Raman spectra of solid and P(VDF-TrFE) porous aerogel films. e,f) Deconvolution of the Raman spectra of solid and P(VDF-TrFE) porous aerogel.

crystalline phases of the material and the effectiveness of the poling step.[42] Therefore, these factors should be able to explain the differences in ferro- and piezoelectric performance of the porous versus solid P(VDF-TrFE).

2.3.1. Crystallinity and Crystalline Phases

PVDF polymer mainly exhibits four types of crystalline phases including α, β, γ, and δ.[43] Among these phases, the β-phase is notable for its significant spontaneous polarization. P(VDF-TrFe), which is formed by incorporating trifluoroethylene (TrFE) units into PVDF, crystallizes readily into the β-phase. The crystallinity of the solid and P(VDF-TrFE) porous aerogel films was studied using X-ray diffraction (XRD). The XRD patterns are illustrated in **Figure** 3a. Notably, the β-phase peak is distinct at $2\theta = 20.1°$ in both cases. The degree of crystallinity of the films can be determined by:

$$X_c\,(\%) = \frac{A_c}{A_A + A_c} \cdot 100 \qquad (2)$$

where A_c represents the peak area of the crystalline phase and A_A denotes the peak area of the amorphous phase.[26] The crystalline and amorphous phase peaks were identified through Gaussian deconvolution of the XRD patterns (Figure 3b,c). The solid P(VDF-TrFE) film exhibits a crystallinity degree of 64.3%, whereas the porous film demonstrates 50.3% (**Table** 2). Therefore, the fabrication process notably influences the crystallinity of the films. This finding also implies that the piezoelectric properties of the P(VDF-TrFE) porous aerogel film may be diminished compared to the solid film.

The Raman spectra of both the solid and P(VDF-TrFE) porous aerogel films were further investigated to quantify the crystalline phase content of these films. Figure 3d illustrates the normalized and smoothed Raman spectra in the wavenumber range from 355 to 1500 cm^1. Generally, the absorption bands associated with 509, 840, 1275, and 1442 cm^{-1} peaks are attributed to the β-phase, while the bands at 795, 880, 975, and 1209 cm^{-1} are characteristic of the α-phase.[43–45] A clear difference between the solid and the porous film´s Raman spectra can be seen, some of the α-phase peaks observed in the solid film spectra are not visible in the porous spectra. However, the proportion of α-phase and β-phase is typically determined by analyzing the

Table 2. Crystallinity and relative fraction of the α-phase and β-phase.

Sample	X_c (%)	α-phase peak at (cm^{-1})	β -phase peak at (cm^{-1})	F(α)	F(β)
Solid P(VDF-TrFE)	64.3%	795	858	11.7%,	88.3%
Porous P(VDF-TrFE)	50.3%	804	841	24.4%	75.6%

© 2024 The Authors. Advanced Functional Materials published by Wiley-VCH GmbH

16163028, 0, Downloaded from https://onlinelibrary.wiley.com/doi/10.1002/adfm.202312881 by Tampere Universitaet Foundation, Wiley Online Library on [23/02/2024]. See the Terms and Conditions (https://onlinelibrary.wiley.com/terms-and-conditions) on Wiley Online Library for rules of use; OA articles are governed by the applicable Creative Commons License

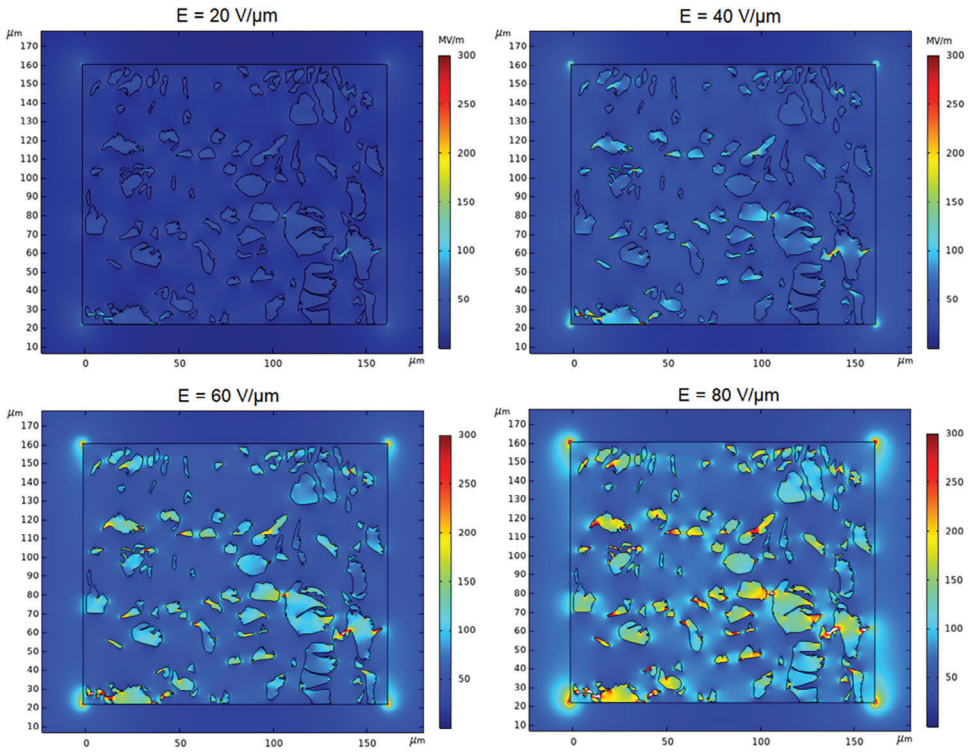

Figure 4. Finite element model of the electric field distribution inside the P(VDF-TrFE) porous aerogel sample during the poling step with applied electric field ranging from 20 to 80 V μm^{-1}.

characteristic peaks of α-phase and β-phase located ≈795 and 840 cm^{1}, respectively.[44–52] For the porous sample, the β-phase peak appears at 841 cm^{-1}, whereas it is shifted by 17 cm^{-1} for the solid. The observed variation in the peak positions can be attributed to the distinct structural characteristics of the films, which involve differences in polarity and crystal morphologies.[45] It should be also noted that the vibrational bands typically associated with the β-phase are the result of the convolution of contributions from multiple sources.[45] Therefore, the amount of α-phase and β-phase can be estimated by deconvolution of the spectra into individual contributions of the overlapping peaks. Figure 3e,f illustrate the decomposed spectra of the solid and porous P(VDF-Tr-Fe) films from 740 to 940 cm^{-1}. The phase fraction of the α-phase (F(α)) and β-phase (F(β)) can be calculated according to:

$$F(\alpha) = \frac{A_\alpha}{A_\alpha + A_\beta} \cdot 100 \quad (3)$$

$$F(\beta) = \frac{A_\beta}{A_\alpha + A_\beta} \cdot 100 \quad (4)$$

where, A_α and A_β represent the integrated area of the associated α-phase and β-phase peaks. Table 2 summarizes the calculated values of F(α) and F(β) for the respective absorption bands. In both cases, the samples show a smaller fraction of α-phase content in comparison to the β-phase.

2.3.2. Effectiveness of the Poling Step

Although the fraction of crystalline to amorphous material, and the fraction of polar β-phase to non-polar α-phase, are both reduced in the case of P(VDF-TrFE) porous aerogel, the relatively small amount of reduction cannot fully explain the observed differences in the P_r value and piezoelectric sensitivity. Therefore, a finite element model for the P(VDF-TrFE) porous aerogel sample was created to study the effectiveness of the poling step. **Figure 4** shows the electric field strength within the sample for applied electric fields of 20, 40, 60, and 80 V μm^{-1} (the ground electrode is the bottom side of the square box, and the voltage electrode is the top side). The most notable feature is the electric field strength difference between the bulk of the P(VDF-TrFE) and the pores: for 20, 40, 60, and 80 V μm^{-1} applied field, the average field strength inside the pores is ≈34, ≈69, ≈103, ≈137 V μm^{-1}, respectively, while inside the bulk, it is on average *less* than the applied electric field. From a poling point of view, this is problematic because the field strength exceeds the dielectric breakdown strength of air inside the pores. Based on previous studies on the dielectric breakdown strength of air versus the length of the air gap,[53,54] and the average vertical diameter of the pores (3–4 μm), we can estimate from the FEM results that 50 to 60 V μm^{-1} applied electric field is sufficient to cause dielectric breakdown of the air and prevent efficient poling of the P(VDF-TrFE) porous aerogel sample. This result is corroborated by the PE-loop measurement results where it was impossible to apply over 60 V μm^{-1} applied field without destroying the sample (see Figure S8, Supporting Information).

© 2024 The Authors. Advanced Functional Materials published by Wiley-VCH GmbH

16163028, 0, Downloaded from https://onlinelibrary.wiley.com/doi/10.1002/adfm.202312881 by Tampere Universitaet Foundation, Wiley Online Library on [23/02/2024]. See the Terms and Conditions (https://onlinelibrary.wiley.com/terms-and-conditions) on Wiley Online Library for rules of use; OA articles are governed by the applicable Creative Commons License

Table 3. Different TENG combinations.

Polarization State	Opposite Material
Non-poled P(VDF-TrFE) porous aerogel	PET
	PI
	Ecoflex
	TPU
Positive-poled P(VDF-TrFE) porous aerogel	PET
	PI
	Ecoflex
	TPU
Negative-poled P(VDF-TrFE) porous aerogel	PET
	PI
	Ecoflex
	TPU

It can be therefore concluded that the differences in ferro- and piezoelectric performance of the porous versus solid P(VDF-TrFE) can be mainly explained by the weak poling step efficiency of the P(VDF-TrFE) porous aerogel and *not* the differences in the crystallinity or β-phase fraction. It is also noteworthy, that engineering smaller pores does not necessarily improve the poling efficiency: although the dielectric breakdown strength of air increases with decreasing gap length (or pore diameter), the field strength also increases accordingly (c.f. increased field intensity in small dimension pores in Figure 4). The engineered porosity seems to therefore result in a fundamental limitation for the utilization of the ferro- and piezoelectric properties of the P(VDF-TrFE).

2.4. Triboelectric Performance of P(VDF-TrFE) Porous Aerogel

P(VDF-TrFE) porous aerogel films, exhibiting different polarization states, were subsequently paired with polymers exhibiting diverse degrees of triboelectricity. This systematic pairing aimed to determine the ideal polarization state of P(VDF-TrFE) for its effective use in triboelectric applications. The analysis was done for the contact pairs listed in **Table 3**. The selected opposite materials were as follows: TPU and PET as tribopositive polymers and Ecoflex and PI as tribonegative polymers.[55–59] The mechanical properties of the selected materials were also considered in addition to their triboelectric property. Consequently, the opposite chosen materials can be also divided into two categories: non-stretchable (i.e., PET and PI), and stretchable (i.e., Ecoflex and TPU). The triboelectric performance of the different contact pairs was evaluated by measuring the open circuit voltage (V_{OC}) and generated charges (Q_O). **Figure 5a–f** illustrate the average generated V_{OC} and Q_O for each contact pair, showcasing the average peak from 600 continuous tapping cycles. The peak voltage value and charge of 115.8 ± 6.5 V and 40.4 ± 1.9 nC were obtained for the contact pair P(VDF-TrFe)/Ecoflex when no poling was applied to the film. In this contact pair, P(VDF-TrFE) acts as tribopositive material owing to its higher position in the triboelectric series in comparison to Ecoflex.[57] As can be seen from Figure 5b,c, the polarization of the porous film resulted in a decrease of the triboelectric output for the contact pair P(VDF-TrFe)/Ecoflex. In both polarization states, the output voltage and generated charges decreased as follows: for the positive poled state to 69.9 ± 2.6 V and 22.7 ± 1.9 nC, and for the negative poled state to 76.3 ±1.6 V and 26.1 ± 0.7 nC. However, for the case when the P(VDF-TrFE) porous aerogel is positively poled and paired with PET, there is an increase of 30.5% in the output voltage and a 23.2% increase in the generated charges. It is also noteworthy that for the P(VDF-TrFE) porous aerogel/PI and P(VDF-TrFE) porous aerogel/TPU contact pairs the output voltage as well as the generated charges are much lower compared to PET and Ecoflex combinations. The ranking of PI in the triboelectric series is closely aligned with PVDF, resulting in a lower transferred charge, whereas Ecoflex, positioned far from PI, exhibits the highest output.[60] Therefore, we concluded that the most beneficial configuration for a TENG is the contact pair non-poled P(VDF-TrFE) porous aerogel/Ecoflex.

Furthermore, the triboelectric performance of the pair P(VDF-TrFE) porous aerogel/Ecoflex was compared with the pair solid P(VDF-TrFe)/Ecoflex to investigate if the absence of piezoelectric response in the P(VDF-TrFE) porous aerogel may have a significant impact on the TENG charge output. When using P(VDF-TrFE) in TENGs, the charge output may be generated through the combination of 1) piezoelectric charges, which are generated due to mechanical deformation of the P(VDF-TrFE), and 2) triboelectric charges, which are generated by friction and contact between the P(VDF-TrFE) and the opposite triboelectric material.[61] Figure 5g,h show the comparison of the open circuit voltage and generated charges of the contact pairs solid P(VDF-TrFE)/Ecoflex and P(VDF-TrFE) porous aerogel for different polarization states. In the case of the solid P(VDF-TrFE), when it is positively poled, the triboelectric output is enhanced by the piezoelectric effect thereby resulting in a higher total charge output (16 nC increase). It is noteworthy, that this high increase cannot be explained simply by the piezoelectric effect, because in this deformation mode, the piezoelectric charge generation is mainly explained by the d_{33}-coefficient which was measured to be only 27 pC N^{-1}. Instead, the increase is likely due to the change in the work function/Fermi levels of the P(VDF-TrFE) caused by the piezoelectric charge which changes the surface charge density (i.e., triboelectric charge).[62] In other words, the piezoelectric effect *amplifies* the triboelectric effect in the case of the solid P(VDF-TrFE) film.

In the case of the P(VDF-TrFE) porous aerogel, similar behavior is not observed, instead, the total charge output is decreased for both poling states. This can be the result of morphological changes in the structure of the film after corona poling (see Figure S8, Supporting Information). However, what is most interesting about the results, is that the non-poled P(VDF-TrFE) porous aerogel results in significantly higher charge output when compared to non-poled solid P(VDF-TrFE). As the piezoelectric effect is absent in both cases (non-poled state), the output is purely due to triboelectric charges and the results therefore indicate a 60 to 70% improvement in the triboelectric charge generation of the P(VDF-TrFE) porous aerogel when compared to the solid film. This is likely because of the higher surface area of the porous film as indicated by the surface roughness measurements (see Section 2.1 2.1).[63] It is noteworthy that the triboelectric output of the non-poled P(VDF-TrFE) porous aerogel is almost the same as the total charge output of the positive poled solid

© 2024 The Authors. Advanced Functional Materials published by Wiley-VCH GmbH

16163028, 0, Downloaded from https://onlinelibrary.wiley.com/doi/10.1002/adfm.202312881 by Tampere Universitaet Foundation, Wiley Online Library on [23/02/2024]. See the Terms and Conditions (https://onlinelibrary.wiley.com/terms-and-conditions) on Wiley Online Library for rules of use; OA articles are governed by the applicable Creative Commons License

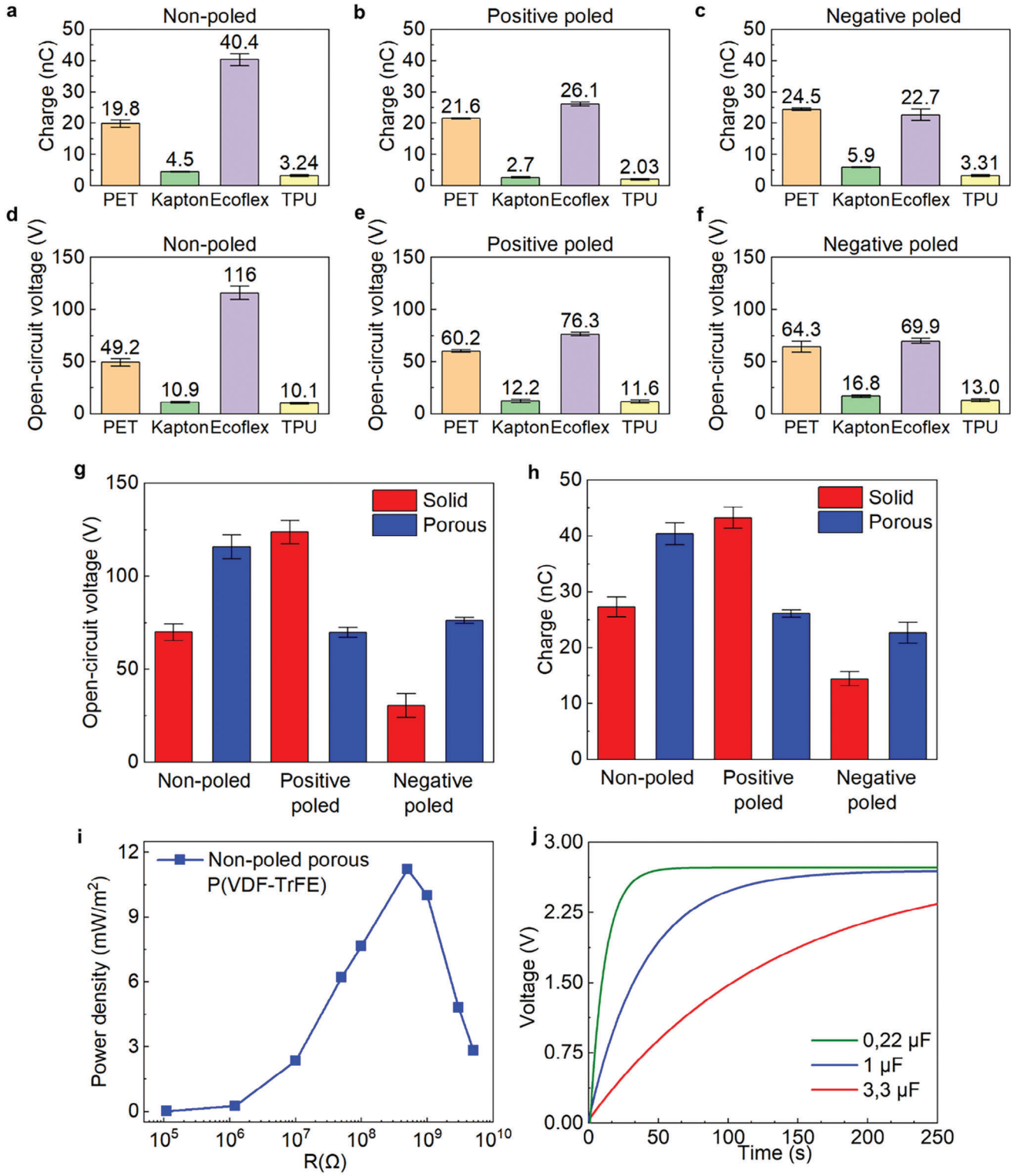

Figure 5. Triboelectric characterization of different TENG contact pairs (listed in Table 3). a–c) Generated charge of TENG contact pairs comprising P(VDF-TrFE) porous aerogel with different polarization states and different opposite triboelectric materials, representation of the average of 600 cycles. d–f) Open-circuit voltage of TENG contact pairs comprising P(VDF-TrFE) porous aerogel with different polarization states and different opposite triboelectric materials, representation of the average of 600 cycles. g) Comparison of the open-circuit voltage of the contact pairs solid P(VDF-TrFE)/Ecoflex and P(VDF-TrFE) porous aerogel for different polarization states. h) Comparison of generated charges of the contact pairs solid P(VDF-TrFE)/Ecoflex and P(VDF-TrFE) porous aerogel for different polarization states. i) Average power density of the non-poled P(VDF-TrFE) porous aerogel/Ecoflex contact pair. j) Charging curves of 0.22, 1, and 3.3 μF capacitors from the contact pair non-poled P(VDF-TrFE) porous aerogel/Ecoflex.

© 2024 The Authors. Advanced Functional Materials published by Wiley-VCH GmbH

16163028, 0, Downloaded from https://onlinelibrary.wiley.com/doi/10.1002/adfm.202312881 by Tampere Universitaet Foundation, Wiley Online Library on [23/02/2024]. See the Terms and Conditions (https://onlinelibrary.wiley.com/terms-and-conditions) on Wiley Online Library for rules of use; OA articles are governed by the applicable Creative Commons License

P(VDF-TrFE). In summary, there is no significant decrease in the energy harvesting performance although the poling step has been omitted and the material stretchability has been greatly enhanced.

The output voltage of the optimum contact pair was measured when connecting an external load to investigate its power generation capabilities. To determine the average power per unit area (P_{ave}) and the maximum instantaneous power per unit area (P_{max}), the following formulas were employed:

$$P_{ave} = \frac{P}{A} = \frac{V_{RMS}^2}{R \cdot A} \quad (5)$$

$$P_{max} = \frac{V_{peak}^2}{R \cdot A} \quad (6)$$

where V_{RMS} is the root mean square voltage, R represents the load resistance, and A denotes the effective area of the TENG. The calculation of V_{RMS} was done using the MATLAB function "*rms*" applied to a voltage signal encompassing 200 cycles. Additionally, the maximum instantaneous power was calculated for the maximum voltage peak value. As the generated output power depends on the impedance matching between the TENG's internal impedance and the external load, the output power was examined for an external load ranging from 110 kΩ to 5 GΩ. Furthermore, to simulate the device's application of harvesting the mechanical energy from human motion, the generated power was evaluated at a very low frequency (0.75 Hz) (human motion is irregular and commonly occurs at such low frequencies[64,65]). Figure 5i illustrates the power density of the non-poled P(VDF-TrFe)/Ecoflex pair. The selected configuration generated an average power density of 11.2 mW m^{-2} and maximum instantaneous power of 86.6 mW m^{-2} for a resistive load of 500 MΩ when applying a force of 66.4 ± 7.6 N at 0.75 Hz. The non-poled P(VDF-TrFE) porous aerogel exhibited a similar instantaneous power compared to its solid counterpart (refer to Figure S10, Supporting Information). Additionally, while still attached to the motorized test stand, the non-poled P(VDF-TrFE) porous aerogel/Ecoflex pair was connected to a full-wave diode bridge to convert the generated AC voltage to DC. Then, capacitors of 0.22, 1, and 3.3 µF were used to store the energy generated by the TENG. Figure 5j illustrates the voltage curve while charging the capacitors. These results indicate that the selected configuration may be used for harvesting energy from human motion. The incorporation of the P(VDF-TrFE) porous aerogel/Ecoflex stack on a fully integrated TENG is presented in the next section.

2.5. Performance of the TENG based on P(VDF-TrFE) Porous Aerogel

An integrated device for energy harvesting is demonstrated based on the P(VDF-TrFE) porous aerogel/Ecoflex pair using the contact-separation configuration (see **Figure** 6a). A detailed summary of the device assembly is presented in Figures S11–S14, Supporting Information). The device was entirely fabricated using stretchable materials, including TPU substrates, Ecoflex, and P(VDF-TrFE) porous aerogel as active layers, and electrodes fabricated with stretchable silver ink.[66–68] This composition inherently grants the device stretchability, utilizing the mechanical characteristics of these materials to ensure overall flexibility and resistance to mechanical deformations. The viability of the use of the integrated TENG for energy harvesting was further studied by applying a periodic compressive force of 63.4 ± 7.2 N at 0.75 Hz. Figure 6b,c show the electrical performance of the device for 100 cycles. The measured output voltage and charge of the presented device were 105.6 ± 10.8 V and 35.8 ± 2.2 nC. The average power density of the integrated TENG follows the same trend as in the results presented in Section 2.4, while the average power density was 9.9 mW m^{-2} and maximum instantaneous power of 62.8 mW m^{-2} for a resistance load of 500 MΩ (Figure 6d). The 12.2% decrease in average power can be attributed to varying test conditions that directly affect the interaction between the triboelectric layers.[69] After the electrical characterization of the device, the energy storage capability of the device was studied. The TENG voltage output was also rectified as in Section 2.4 and directly stored by a capacitor. Figure 6f illustrates the capacitor charging capability of the device. Additionally, a 3.3 µF capacitor was charged by tapping the TENG with a finger reaching a charging voltage of ≈3 V. The energy harvested by the TENG and stored in the capacitor was subsequently used to illuminate four LEDs in parallel connected in parallel (Figure 6g; Movie S1, Supporting Information). This demonstration showcases the device's capability in real-time energy applications, validating its potential for practical use in powering low-energy electronics.

3. Conclusion

A fully printed TENG based on P(VDF-TrFE) porous aerogel has been demonstrated in this study. We have developed P(VDF-TrFE) porous aerogel films to enhance the stretchability and improve the triboelectric performance of P(VDF-TrFE) when no poling is applied. We systematically investigated the impact of this porous structure on the material's mechanical, ferroelectric, and triboelectric properties by direct comparison with equivalent solid P(VDF-TrFE) film. Our findings revealed distinct differences between the porous and solid P(VDF-TrFE) films. The porous film exhibited significantly improved stretchability compared to the solid film, making it a promising candidate for applications requiring stretchable and deformable materials. However, the P(VDF-TrFE) porous aerogel film had lower ferro- and piezoelectric performance compared to the solid film. This decrease in performance was attributed to the inefficient poling of the porous material, primarily due to the dielectric breakdown of air within the pores during the poling process. Despite this, our study demonstrated that the non-poled P(VDF-TrFE) porous aerogel/Ecoflex contact pair exhibited favorable triboelectric performance, making it suitable for energy harvesting applications. We successfully integrated this contact pair into a fully printed TENG device showing a voltage of 105.6 ± 10.8 V, a charge of 35.8 ± 2.2 nC, peak power of 62.8 mW m^{-2} and an average power of 9.9 mW m^{-2} over 100 tapping cycles at 0.75 Hz. The TENG showed potential for harvesting energy from human motion to power low-energy electronics. In conclusion, the engineered P(VDF-TrFE) porous aerogel films offer improved stretchability and triboelectric properties, with potential applications in flexible and stretchable energy harvesting devices.

© 2024 The Authors. Advanced Functional Materials published by Wiley-VCH GmbH

16163028, 0, Downloaded from https://onlinelibrary.wiley.com/doi/10.1002/adfm.202312881 by Tampere Universitaet Foundation, Wiley Online Library on [23/02/2024]. See the Terms and Conditions (https://onlinelibrary.wiley.com/terms-and-conditions) on Wiley Online Library for rules of use; OA articles are governed by the applicable Creative Commons License

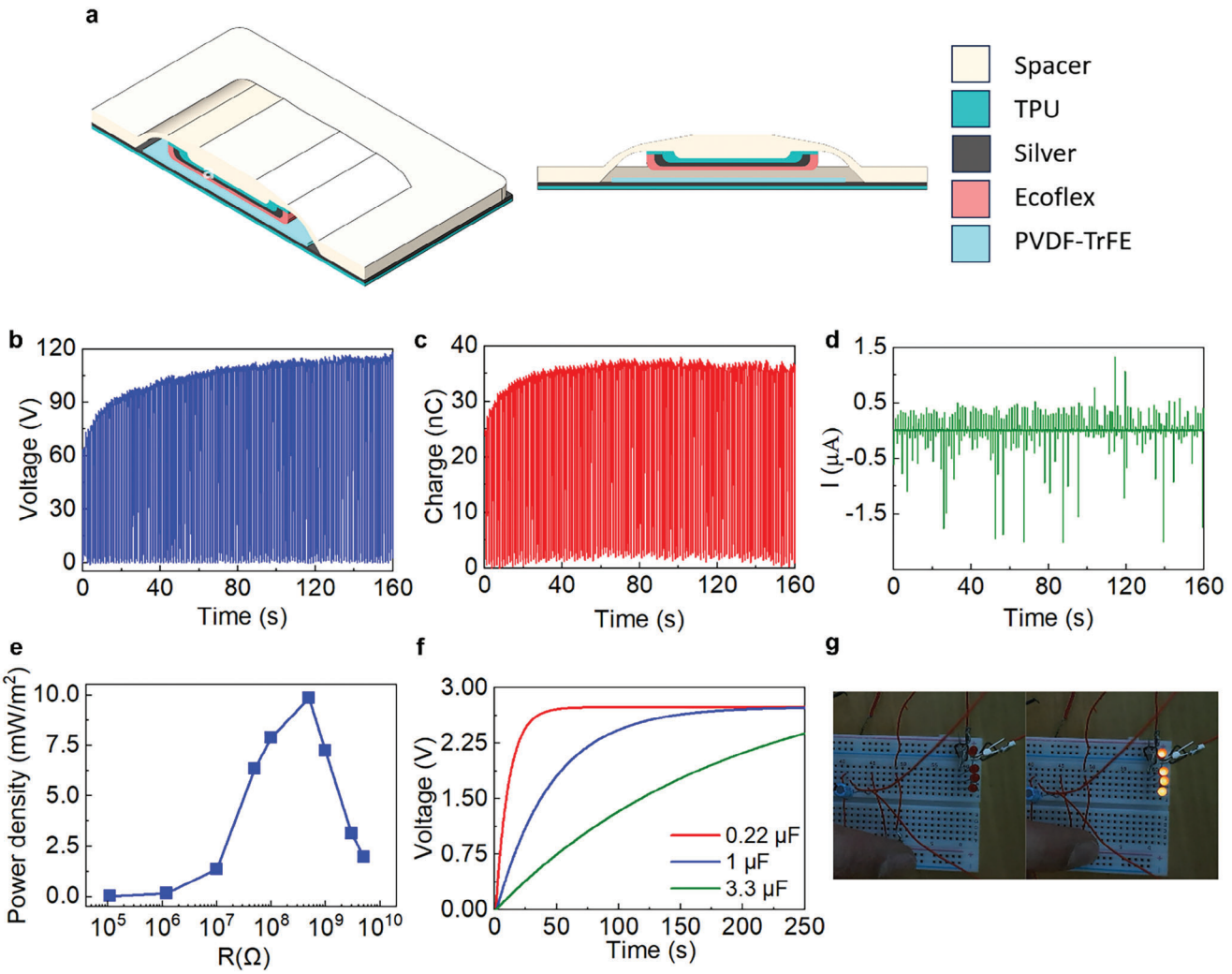

Figure 6. Triboelectric characterization of the fabricated TENG based on contact-separation mode. a) Schematic of the cross-section view of the TENG. b–d) TENG's open circuit voltage, generated charges, short-circuit current. e) Average power density of the TENG. f) Charging curves of 0.22, 1, and 3.3 μF capacitors from the TENG. g) LEDs connected in parallel for power generation demonstration.

4. . Experimental Section

Fabrication of Porous and Solid P(VDF-TrFE) Film: P(VDF-TrFE) powder (FC 20, Arkema Piezotech) was dissolved in DMSO with a polymer concentration of 11 wt.%. The solution was kept under mechanical stirring for 4 h at 60 °C. Electrodes were inkjet-printed (DMP-2801, Fujifilm Dimatix) with a 10 pl cartridge using silver (Ag) nanoparticle ink (DGP 40LT-15C, Advanced Nanoproducts) on a PET foil (Melinex ST506, DuPont) with a thickness of 125 μm. Then, the deposition of the P(VDF-TrFE) solution on top of the electrodes was done using an automatic blade coater (Motorized Film Applicator CX4, MTV Messtechnik). The P(VDF-TrFE) layer was patterned using a PET mask. To support the following process description, the process flow diagram for the fabrication of porous and solid P(VDF-TrFE) films is also presented in the Supplementary Information (Figures S1–S5, Supporting Information). To obtain solid a P(VDF-TrFE) film, the samples were annealed after the blade coating process at 120°C in a convection oven for 1 h. To obtain a P(VDF-TrFE) porous aerogel film, the post-treatment process (i.e., after blade coating) was divided into two stages. First, the samples were frozen immediately after the P(VDF-TrFE) deposition. This was done by placing the PET foil on top of pre-cooled metallic plates (−19 °C), which caused the P(VDF-TrFE) solution to freeze immediately from bottom up (i.e., unidirectional freezing); this was followed by placing the samples in the conventional freezer (−19 °C) overnight to guarantee the complete solvent crystallization. It is noteworthy that in this study unidirectional freezing of the P(VDF-TrFE) solution was achieved at −19 °C while in previously reported studies liquid nitrogen (LN_2) has been used for directional freezing.[39] After the freezing process, the samples were immersed in a DI water bath to remove the solvent,[39] this step was repeated 4 times. Once the DMSO was removed, the samples were again frozen. Then, the samples were freeze-dried for 25 h to remove any excess water. Finally, the samples were annealed at 120 °C in a convection oven for 1 h (similar to solid P(VDF-TrFE) film).

Polarization of P(VDF-TrFE): The contact poling process of the piezoelectric material was done with the ferroelectric characterization tool (aixACCT TF2000, aixACCT Systems GmbH) coupled with a high-voltage amplifier (610C, TREK). In this case, poly(3,4-ethylenedioxythiophene) polystyrene sulfonate (PEDOT:PSS) (Clevios P Jet 700, Heraeus) electrodes were inkjet-printed on a separate PET sheet which was then placed in direct contact with the surface of the P(VDF-TrFE) films. The system generates a pre-pole signal followed by three bipolar triangular signals used for poling. Each signal was followed by 1 s relaxation time, and the signal frequency was set to 2.5 Hz. In addition to contact poling, the poling of the P(VDF-TrFE) porous aerogel was also done using corona poling. In this scenario, a conductive film (aluminum foil) was fixed above the

© 2024 The Authors. Advanced Functional Materials published by Wiley-VCH GmbH

16163028, 0, Downloaded from https://onlinelibrary.wiley.com/doi/10.1002/adfm.202312881 by Tampere Universitaet Foundation, Wiley Online Library on [23/02/2024]. See the Terms and Conditions (https://onlinelibrary.wiley.com/terms-and-conditions) on Wiley Online Library for rules of use; OA articles are governed by the applicable Creative Commons License

P(VDF-TrFE) porous aerogel film to ensure an even distribution of the applied electric field (3 kV). The distance between the surface of the P(VDF-TrFE) film and the conductive film was 1 mm. This setup is shown in Figure S7 (Supporting Information). In all cases, the bottom electrode was fabricated as described in Fabrication of Porous and Solid P(VDF-TrFE) Film. Figure 2a,b illustrate the poling configurations used in this study.

Opposite Triboelectric Material Selection: To select the optimized triboelectric pair, four materials (two flexible and two stretchable) were selected for the opposite triboelectric layer: PET, PI (Kapton, DuPont), TPU (U4201, Epurex Platilon), and Ecoflex (00-30, Smooth-On, Inc). The thickness of each material is presented in Table S1 (Supporting Information). Silver electrodes were inkjet-printed on PET and PI as described in Fabrication of Porous and Solid P(VDF-TrFE) Film. Because printing directly on Ecoflex proved to be difficult, the following approach was adopted: part A and part B of Ecoflex were mixed at the ratio of 1:1, and subsequently blade-coated on an inkjet-printed silver electrode having PET as substrate. In the case of TPU, the electrodes were blade-coated using a stretchable silver flake paste (CI-1036, Nagase ChemteX America Corp). Thin cables for measurement were mounted and fixed to the electrodes using PEDOT:PSS ink paste (Clevios S V4 STAB, Heraeus).

Triboelectric Nanogenerator (TENG) Layers Fabrication: A 100 µm thick TPU film laminated on PET was used as substrate. The electrodes were made using stretchable silver flake paste (CI-1036). The deposition of the ink was done using an automatic blade coater and patterned using a 50 µm thick PI mask. The electrode dimensions were 45 mm x 45 mm. The fabrication of the P(VDF-TrFE) porous aerogel was done following the process explained in 2.1. The dimensions of the porous layer were 35 mm x 35 mm, and the solution was printed such that it only touched the electrode material thereby preventing the dissolution of TPU by the DMSO (see Figure S11, Supporting Information for reference). Ecoflex, as the opposite triboelectric material, was blade-coated on top of a silver electrode and cured at 120°C for 30 min. Thin cables for measurement were mounted and fixed to the electrodes using PEDOT:PSS ink paste.

3D Printed Spacer: Fused deposition modeling (FDM) printing technique was used to fabricate the TENG spacer. A TPU filament (95A, Ultimaker) was 3D printed using a desktop printer (Ultimaker 3, Ultimaker). The printed speed was 25 mm s^{-1} and it was plated at room temperature. The printing design contained a skirt consisting of two lines to ensure that the material flowed homogeneously. In addition, the slicing of the model was made using the UltiMaker Cura software in which a gyroid-type infill pattern with a density of 8% was used to ensure flexibility and some stretchability. The spacer consists of two-leveled structures, where the lower level is composed of a hollow square section of 50 mm outer part, 30 mm long inner part, and 2 mm thick, and the upper level consists of a square 30 mm side and 2 mm thick with curved edges connected to the lower level by curved paths located on parallel sides (see Figure 6a). In addition, a rectangle section (15 mm high, 20 mm long, and 1 mm thick) is located on the inner surface of the upper level to ensure contact area between the opposite layers of the TENG.

Device Integration: The 3D-printed spacer was treated with oxygen plasma for 1 min. A thin adhesive film (Printable Tattoo Paper, Silhouette) was used to attach the TENG layers to the spacer. First, the TPU/Ag/Ecoflex stack was laminated to the inner surface of the upper level of the 3D-printed spacer (see Figures S11,S12, Supporting Information). The TPU/Ag/P(VDF-TrFE) stack was then attached to the lower level of the spacer facing the TPU/Ag/Ecoflex stack. Figures S13,S14 (Supporting Information) show the top and side view of the fabricated device.

Material Characterization: The surface image of the solid and P(VDF-TrFE) porous aerogel films was obtained using SEM. Additionally, the surface profile of the films was measured using a stylus profilometer (Dektak XT, Bruker). The weights of the fabricated films were measured using a high-precision laboratory scale. The XRD of the samples was measured with an X-ray diffractometer (Empyrean, Panalytical). The Raman spectroscopy of the films was measured with a confocal Raman microscopy (inVia Raman microscope, Renishaw) using a 785 nm laser beam. The quantitative analysis of the XRD and Raman spectra was done using the software Origin (2019, OriginLab). For the XRD spectra analysis, the measured spectra were deconvoluted into the sum of the amorphous and crystalline phase peaks using a Gaussian function distribution.[26] For the Raman spectra analysis, the measured spectra were deconvoluted using the pseudo-Voigt function distribution to identify the crystalline phase peaks (i.e., α- and β-phase). The mechanical properties of the fabricated films were studied using a motorized tension/compression test stand (ESM303, Mark-10). Free-standing films of solid and P(VDF-TrFE) porous aerogel were cut into rectangular pieces of 80 mm x 50 mm and stretched uniaxially. The films were fixed between two clamps with a length of 22.2 mm (Figure S6a,b, Supporting Information). The tensile test was performed at a strain rate of 50 mm min^{-1} and initial zero load.

Electrical Characterization: The triboelectric performance of the samples was tested using the contact-separation principle. A motorized tension/compression test stand (ESM303, Mark-10) was used to provide mechanical motion. The triboelectric layer containing P(VDF-TrFE) was attached to the bottom plate of the test stand and the opposite triboelectric layer to the upper plate. The travel speed was set to 1100 mm min^{-1} and the zero position of the upper plate was configured to have a 2 mm distance between the triboelectric layers. The applied force and displacement were recorded using MESURgauge Plus (Mark-10) software. The open-circuit voltage, short-circuit current, and generated charges were monitored using an electrometer (6517B, Keithley). A MATLAB script was used to configure the electrometer and to record the real-time measurements. Figure S9 (Supporting Information) illustrates the whole setup. The energy harvesting capabilities of the developed TENG were evaluated by charging commercial capacitors of 0.22, 1, and 3.3 µF. Electrical energy generated by human motion was used to charge a 3.3 µF capacitor and illuminate 4 commercial LEDs connected in parallel (rated 1.6 V and 1 mA).

Finite Element Model of the Poling Step: COMSOL Multiphysics (v.5.6.) was used to generate the 2D FE model for the electric field distribution inside the P(VDF-TrFE) porous aerogel during the poling step. The relative permittivity of the air (pores) was assumed to be 1.0 while for P(VDF-TrFE) following relative permittivity matrix was used:[70]

$$\begin{bmatrix} \varepsilon_{r11} & & \\ & \varepsilon_{r21} & \\ & & \varepsilon_{r33} \end{bmatrix} = \begin{bmatrix} 7.9 & & \\ & 7.1 & \\ & & 7.9 \end{bmatrix} \quad (7)$$

The geometry of the porous sample was generated from the SEM image using ImageJ software (National Institutes of Health) and then imported to COMSOL as a CAD file.

Supporting Information

Supporting Information is available from the Wiley Online Library or from the author.

Acknowledgements

This work made use of Tampere Microscopy Center facilities. The authors would also like to thank Leo Hyvärinen for the XRD measurements, Chirag Mevada for the SEM images at Tampere University, and the High Voltage Laboratory from Tampere University for support with equipment. K.L.M would like to thank Walter Ahlström Foundation, the Tutkijat Maailmalle program, and Tekniikan edistämissäätiö for support. K.L.M would also like to thank Yong Ding at the Georgia Institute of Technology for support during her research visit. M.M.L. would like to acknowledge the financial support by H2020 Marie Skłodowska-Curie Actions (MSCA) Individual Fellowship (IF) Grant UNOPIEZO (Grant No. 10102243) and also thank Walter Ahlström Foundation and the Tutkijat Maailmalle program. The research used Research Infrastructures "Printed Intelligence Infrastructure" (PII-FIRI, Academy of Finland Grant 320019).

Conflict of Interest

The authors declare no competing interests.

© 2024 The Authors. Advanced Functional Materials published by Wiley-VCH GmbH

16163028, 0, Downloaded from https://onlinelibrary.wiley.com/doi/10.1002/adfm.202312881 by Tampere Universitaet Foundation, Wiley Online Library on [23/02/2024]. See the Terms and Conditions (https://onlinelibrary.wiley.com/terms-and-conditions) on Wiley Online Library for rules of use; OA articles are governed by the applicable Creative Commons License

Author Contributions

K.L.M. conceptualized the idea for the study; designed methodology; performed validation, formal analysis, investigation, and acquisition of resources; wrote the original draft; and visualized the idea for the study. R.C.G. acquired resources; wrote, reviewed, and edited the final manuscript. A.T. acquired resources, and wrote, reviewed, and edited the final manuscript. H.Z. conceptualized the idea for the study; wrote, reviewed, and edited the final manuscript. Z.L.W. wrote, reviewed, and edited the final manuscript. M.M. conceptualized the idea for the study; performed formal analysis; wrote, reviewed, and edited the final manuscript; and performed supervision. M.-M.L. conceptualized the idea for the study; designed methodology; performed formal analysis; acquired resources; wrote, reviewed, and edited the final manuscript, and performed supervision.

Data Availability Statement

The data that support the findings of this study are available from the corresponding author upon reasonable request.

Keywords

3D printing, additive manufacturing, energy harvesting, P(VDF-TrFE), piezoelectric, printed electronics, triboelectric

Received: October 18, 2023
Revised: December 29, 2023
Published online:

[1] A. S. Farooq, P. Zhang, *Sens. Actuators Phys.* **2022**, *344*, 113715.
[2] Md. N. Hasan, S. Sahlan, K. Osman, M. S. Mohamed Ali, *Adv. Mater. Technol.* **2021**, *6*, 2000771.
[3] F. R. Fan, W. Tang, Z. L. Wang, *Adv. Mater.* **2016**, *28*, 4283.
[4] M. Liu, F. Qian, J. Mi, L. Zuo, *Appl Energy* **2022**, *321*, 119379.
[5] Z. L. Wang, G. Zhu, Y. Yang, S. Wang, C. Pan, *Mater. Today.* **2012**, *15*, 532.
[6] S. Solanki, A. K. Gupta, U. Saha, A. V. Krasnoslobodtsev, R. K. Gupta, B. D. Malhotra, *Sustain. Energy Technol. Assess.* **2023**, *57*, 103233.
[7] Y. W. Kim, H. B. Lee, J. Yoon, S.-H. Park, *Nano Energy* **2022**, *95*, 107051.
[8] M. He, W. Du, Y. Feng, S. Li, W. Wang, X. Zhang, A. Yu, L. Wan, J. Zhai, *Nano Energy* **2021**, *86*, 106058.
[9] X. Zhang, Z. Li, W. Du, Y. Zhao, W. Wang, L. Pang, L. Chen, A. Yu, J. Zhai, *Nano Energy* **2022**, *96*, 107115.
[10] M. J. Cima, *Nat. Biotechnol.* **2014**, *32*, 642.
[11] Y. Zhou, W. Deng, J. Xu, J. Chen, *Cell Rep Phys Sci* **2020**, *1*, 100142.
[12] W. Kim, T. Okada, H.-W. Park, J. Kim, S. Kim, S.-W. Kim, S. Samukawa, D. Choi, *J Mater Chem* **2019**, *7*, 25066.
[13] J.-H. Lee, H.-J. Yoon, T. Y. Kim, M. K. Gupta, J. H. Lee, W. Seung, H. Ryu, S.-W. Kim, *Adv. Funct. Mater.* **2015**, *25*, 3203.
[14] Z. Zhao, Y. Dai, S. X. Dou, J. Liang, *Mater. Today Energy.* **2021**, *20*, 100690.
[15] J. Fu, Y. Hou, M. Zheng, M. Zhu, *ACS Appl Mater Interfaces* **2020**, *12*, 9766.
[16] K. Lozano Montero, M.-M. Laurila, M. Mäntysalo, *IEEE J. Flex. Electron.* **2022**, *1*, 24.
[17] P. Yadav, T. D. Raju, S. Badhulika, *ACS Appl. Electron. Mater.* **2020**, *2*, 1970.
[18] J. Fu, X. Xia, G. Xu, X. Li, Y. Zi, *ACS Nano* **2019**, *13*, 13257.
[19] Z. Zhou, C. You, Y. Chen, W. Xia, N. Tian, Y. Li, C. Wang, *Org. Electron.* **2022**, *105*, 106491.
[20] R. D'anniballe, A. Zucchelli, R. Carloni, *Sens. Actuators Phys.* **2022**, *333*, 113255.
[21] S. Yu, Y. Zhang, Z. Yu, J. Zheng, Y. Wang, H. Zhou, *Nano Energy* **2021**, *80*, 105519.
[22] S. M. S. Rana, M. T. Rahman, M. Salauddin, S. Sharma, P. Maharjan, T. Bhatta, H. Cho, C. Park, J. Y. Park, *ACS Appl Mater Interfaces* **2021**, *13*, 4955.
[23] Y. Kim, X. Wu, C. Lee, J. H. Oh, *ACS Appl Mater Interfaces* **2021**, *13*, 36967.
[24] N. Sharma, M. Shamkuwar, I. Singh, *Internet of Things and Big Data Analytics for Smart Generation*, (Eds: V. E. Balas, V. K. Solanki, R. Kumar, M. Khari), pp. 27–51. Springer International Publishing, Cham **2019**.
[25] J. Jan, J. Zhu, J. Ting, A. C. Arias, *Adv. Funct. Mater.* **2022**, *32*, 2112343.
[26] R. I. Haque, R. Vié, M. Germainy, L. Valbin, P. Benaben, X. Boddaert, *Flex. Print. Electron.* **2015**, *1*, 015001.
[27] A. H. Espera, J. R. C. Dizon, Q. Chen, R. C. Advincula, *Prog. Addit. Manuf.* **2019**, *4*, 245.
[28] X. Cao, H. Chen, X. Gu, B. Liu, W. Wang, Y. Cao, F. Wu, C. Zhou, *ACS Nano* **2014**, *8*, 12769.
[29] Y. Khan, A. Thielens, S. Muin, J. Ting, C. Baumbauer, A. C. Arias, *Adv. Mater.* **2020**, *32*, 1905279.
[30] M. Sun, J. O. Hill, *J. Biomech.* **1993**, *26*, 229.
[31] W. Kim, H. J. Hwang, D. Bhatia, Y. Lee, J. M. Baik, D. Choi, *Nano Energy* **2016**, *21*, 19.
[32] C. Qian, L. Li, M. Gao, H. Yang, Z. Cai, B. Chen, Z. Xiang, Z. Zhang, Y. Song, *Nano Energy* **2019**, *63*, 103885.
[33] H.-Y. Mi, X. Jing, Q. Zheng, L. Fang, H.-X. Huang, L.-S. Turng, S. Gong, *Nano Energy* **2018**, *48*, 327.
[34] L. Zhang, Y. Liao, Y.-C. Wang, S. Zhang, W. Yang, X. Pan, Z. L. Wang, *Adv. Funct. Mater.* **2020**, *30*, 2001763.
[35] Q. Zheng, L. Fang, H. Guo, K. Yang, Z. Cai, M. A. B. Meador, S. Gong, *Adv. Funct. Mater.* **2018**, *28*, 1706365.
[36] M. Kim, C. Choi, J. P. Lee, J. Kim, C. Cha, *Small* **2022**, *18*, 2107316.
[37] C. Luo, H. Ma, H. Yu, Y. Zhang, Y. Shao, B. Yin, K. Ke, L. Zhou, K. Zhang, M.-B. Yang, *ACS Sustainable Chem. Eng.* **2023**, *11*, 9424.
[38] A. D. Roberts, S. Wang, X. Li, H. Zhang, *J Mater Chem* **2014**, *2*, 17787.
[39] Y. Zhang, C. R. Bowen, S. Deville, *Soft Matter* **2019**, *15*, 825.
[40] C. Han, H. Zhang, Q. Chen, T. Li, L. Kong, H. Zhao, L. He, *Chem. Eng. J.* **2022**, *450*, 138280.
[41] Y. Zhang, X. Guo, W. Wang, L. Chen, L. Liu, H. Liu, Y. He, *IEEE Sens. J.* **2020**, *20*, 14118.
[42] A. Aliane, M. Benwadih, B. Bouthinon, R. Coppard, F. Domingues-Dos Santos, A. Daami, *Org. Electron.* **2015**, *25*, 92.
[43] X. Cai, T. Lei, D. Sun, L. Lin, *RSC Adv.* **2017**, *7*, 15382.
[44] A. Milani, C. Castiglioni, S. Radice, *J Phys Chem B* **2015**, *119*, 4888.
[45] A. Arrigoni, L. Brambilla, C. Bertarelli, G. Serra, M. Tommasini, C. Castiglioni, *RSC Adv.* **2020**, *10*, 37779.
[46] T. Sharma, S.-S. Je, B. Gill, J. X. J. Zhang, *Sens. Actuator A Phys.* **2012**, *177*, 87.
[47] S. Wang, H.-Q. Shao, Y. Liu, C.-Y. Tang, X. Zhao, K. Ke, R.-Y. Bao, M.-B. Yang, W. Yang, *Compos. Sci. Technol.* **2021**, *202*, 108600.
[48] Q. Yao, L. Xie, X. Guo, X. Duan, Y. Li, F. Yu, X. Zhao, *IEEE Sens. J.* **2023**, *23*, 15660.
[49] H.-J. Chen, S. Han, C. Liu, Z. Luo, H.-P. D. Shieh, R.-S. Hsiao, B.-R. Yang, *Sens. Actuators Phys.* **2016**, *245*, 135.
[50] A. Mayeen, K. M. S., M. S. Jayalakshmy, S. Thomas, D. Rouxel, J. Philip, R. N. Bhowmik, N. Kalarikkal, *Dalton Trans.* **2018**, *47*, 2039.
[51] E. H. Abdelhamid, O. D. Jayakumar, V. Kotari, B. P. Mandal, R. Rao, V. M. Naik, R. Naik, A. K. Tyagi, *RSC Adv.* **2016**, *6*, 20089.
[52] D. Chapron, F. Rault, A. Talbourdet, G. Lemort, C. Cochrane, P. Bourson, E. Devaux, C. Campagne, *J. Raman Spectrosc.* **2021**, *52*, 1073.

© 2024 The Authors. Advanced Functional Materials published by Wiley-VCH GmbH

16163028, 0, Downloaded from https://onlinelibrary.wiley.com/doi/10.1002/adfm.202312881 by Tampere Universitaet Foundation, Wiley Online Library on [23/02/2024]. See the Terms and Conditions (https://onlinelibrary.wiley.com/terms-and-conditions) on Wiley Online Library for rules of use; OA articles are governed by the applicable Creative Commons License

[53] F. W. Strong, J. L. Skinner, P. M. Dentinger, N. C. Tien, Proc. SPIE 6111, Reliability, Packaging, Testing, and Characterization of MEMS/MOEMS V, SPIE, Bellingham, WA January **2006**.
[54] R. Gerson, T. C. Marshall, *J. Appl. Phys.* **2004**, *30*, 1650.
[55] W. Zhang, Q. Liu, S. Chao, R. Liu, X. Cui, Y. Sun, H. Ouyang, Z. Li, *ACS Appl Mater Interfaces* **2021**, *13*, 42966.
[56] R. Riaz, B. Dudem, M. A. Costa Angeli, A. Douaki, M. Ahmad, A. Mejia-Aguilar, R. Monsorno, P. Lugli, S. R. P. Silva, L. Petti, *Adv. Mater. Technol.* **2023**, *8*, 2202106.
[57] J. S. C. Koay, W. C. Gan, A. E. Soh, J. Y. Cheong, K. C. Aw, T. S. Velayutham, *J Mater Chem* **2020**, *8*, 25857.
[58] C. Li, P. Wang, D. Zhang, *Nano Energy* **2023**, *109*, 108285.
[59] S. Hu, J. Weber, S. Chang, G. Xiao, J. Lu, J. Gao, W. Jiang, Y. Zhang, Y. Tao, *Adv. Mater. Technol.* **2022**, *7*, 2200186.
[60] H. Zou, Y. Zhang, L. Guo, P. Wang, X. He, G. Dai, H. Zheng, C. Chen, A. C. Wang, C. Xu, Z. L. Wang, *Nat. Commun.* **2019**, *10*, 1427.
[61] D. G. Jeong, Y. J. Ko, J. H. Kim, D. S. Kong, Y. C. Hu, D. W. Lee, S. H. Im, J. Lee, M. S. Kim, G.-H. Lee, C. W. Ahn, J. R. Ahn, M. Lee, J. Y. Park, J. H. Jung, *Nano Energy* **2022**, *103*, 107806.
[62] H. Zou, L. Guo, H. Xue, Y. Zhang, X. Shen, X. Liu, P. Wang, X. He, G. Dai, P. Jiang, H. Zheng, B. Zhang, C. Xu, Z. L. Wang, *Nat. Commun.* **2020**, *11*, 2093.
[63] Y. Zou, J. Xu, K. Chen, J. Chen, *Adv. Mater. Technol.* **2021**, *6*, 2000916.
[64] C. He, B. D. Chen, T. Jiang, L. Xu, C. B. Han, G. Q. Gu, Z. L. Wang, *Adv. Mater. Technol.* **2018**, *3*, 1700251.
[65] C. Hou, T. Chen, Y. Li, M. Huang, Q. Shi, H. Liu, L. Sun, C. Lee, *Nano Energy* **2019**, *63*, 103871.
[66] J. Suikkola, T. Björninen, M. Mosallaei, T. Kankkunen, P. Iso-Ketola, L. Ukkonen, J. Vanhala, M. Mäntysalo, *Sci. Rep.* **2016**, *6*, 25784.
[67] Y. Jiang, Y. Wang, Y. K. Mishra, R. Adelung, Y. Yang, *Adv. Mater. Technol.* **2018**, *3*, 1800248.
[68] T. Salo, D. Di Vito, A. Halme, J. Vanhala, *Micromachines* **2022**, *13*, 1732.
[69] S. Niu, S. Wang, L. Lin, Y. Liu, Y. S. Zhou, Y. Hu, Z. L. Wang, *Energy Environ. Sci.* **2013**, *6*, 3576.
[70] M.-M. Laurila, K. L. Montero, M. Mäntysalo, *Flex. Print. Electron.* **2023**, *8*, 015006.

© 2024 The Authors. Advanced Functional Materials published by Wiley-VCH GmbH

16163028, 0, Downloaded from https://onlinelibrary.wiley.com/doi/10.1002/adfm.202312881 by Tampere Universitaet Foundation, Wiley Online Library on [23/02/2024]. See the Terms and Conditions (https://onlinelibrary.wiley.com/terms-and-conditions) on Wiley Online Library for rules of use; OA articles are governed by the applicable Creative Commons License